Chapter 5

Segregation kinetics of binary polymer fluids: effect of external shear

5.1 Introduction

Polymer blend systems attract considerable research interest due to their broad applications. The kinetics of phase segregation in polymer fluids has been a key research focus for decades [175]. In polymer blend systems, mixing different polymer chains regulates their evolution morphology and, thus, functional properties, providing significant advantages for academic and industrial research. These blends find applications in diverse areas such as electronics [176], textiles [177], and food packaging [178] industries. Specifically, in the biomedical field, they are utilized in drug delivery [179], biodegradable systems [180], as excipients [179], film coatings [181], capsule cells, controlled release tablets [181], and solid dispersions [182], etc. Various theoretical and experimental studies have been conducted on the phase segregation kinetics of polymer blends [183,184] as well as polymers in solution [23]. These investigations typically follow the temperature

quench of polymer fluids from the one-phase region of the phase diagram [185]. Cahn and Hilliard [186] were pioneers in the theoretical study of this process for binary metal alloys. Their work was subsequently extended to polymeric systems by Gennes [187], Pincus [188], and Binder [189], incorporating the well-known Flory-Huggins [190] theory. Phase separation kinetics have been further explored through various experiments under different external conditions and systems. For instance, the study of microemulsions with varying compositions was conducted by Buil et al. [191,192], who discussed the nucleation and growth stages. Additionally, the spinodal decomposition in polymer blends was examined by Hashimoto et al. [85,192] and Hayashi et al. [86,192] using two-step quenching.

The study of polymer mixtures under external influences such as shear flow, elongation flow, temperature, and pressure has become the subject of numerous investigations [193,194]. When shear is applied, mixing and demixing occur in the system, depending on the molecular characteristics of the polymers involved [195,196]. Shear induces microstructural changes in polymer fluids, leading to polymer deformation, concentration fluctuations, and changes in interfacial characteristics [197]. Additionally, shear causes dispersed droplet deformation and breakup, which can be reversible upon the cessation of shear [197,198]. Various experimental works have been focused on the detailed mechanisms behind the formation of elongated strings [199] and elongated droplets [197] under the influence of shear during the homogenization of critical and off-critical polymer mixtures. Using small-angle light scattering and optical microscopy, Keestra et al. [200] have studied the development of anisotropic structures in polymer blends. Fasheng et al. [201] have studied the shift in phase boundary under the influence of shear. Using the experimental methods, the formation of string-like structures of nanoparticles is also analyzed in polymer thin films [202].

The final properties of polymeric fluids depend on their morphological arrangements, which can be tuned by various methods [203–205]. Shear is one of the intriguing effects that can alter final morphologies, involving the orientation of domains [206,207] The orientation of domains depends on various parameters such as shear field, interfacial tension, and viscosity ratio between different phases [208,209]. Ultimately, the effect of shear results in the formation of string-like phase-separated structures with primary axes oriented along the direction of flow [196–199]. At high shear rates, deformation and reorientation in polymer fluids occur due to the softening of interfacial tension between the two phases [210].

Various experimental and theoretical studies based on the shear effect on polymer blends [197,211,212] mainly focused on the linearized theory of Cahn, Hilliard, and Cook [186,213,214] and investigated the formation of different anisotropic structures aligned along a particular direction. Some DPD [215–217] and MD [218,219] simulation studies have analyzed the effect of shear in polymer fluids. They investigated the interfacial properties and the impact of shear on nanoparticles. To the best of our knowledge, the kinetics of phase separation in polymer blends under the effect of shear has not yet been explored. In our recent work [64] discussed in chapter 4, we have studied the influence of external shear on phase segregation kinetics of BCP melt system in bulk. In the present chapter, we extend the same work to the polymer blend system confined between two solid walls with an amorphous arrangement. The shear effect is studied in critical and off-critical polymer blend systems with equal polymer chain lengths. A specific velocity is imparted to the walls in a particular direction to apply shear to the system. Both types of polymer chains have similar interactions with the walls; thus, both types of chains experience a similar effect of shear. We utilized DPD simulation to investigate the shear effect on domain coarsening, scaling properties, growth kinetics, and structural anisotropy.

5.2 System details

We have taken AB polymer blend inside a cubic box of dimensions $L_x \times L_y \times L_z = 64 \times 64 \times 64$ (dimensionless unit) with $\rho = 3$. Thus, the number of DPD beads present in the system is $N = \rho L^3 = 3 \times 64^3 = 7,86,432$. We have considered: (i) the critical polymer blend with an equal ratio of A and B beads ($A : B = 1 : 1$), and (ii) the off-critical blend ($A : B = 3 : 1$). The equal polymer chain length of $N_p = 32$ (degree of polymerization) is taken in both systems. Therefore, in the critical polymer blend system, the number of A and B beads are $N_A = N_B = 3,80,928$; the corresponding volume fractions are $\phi_A = \phi_B = 4.843 \times 10^{-1}$, and the number densities are $\rho_A = \rho_B = 1.453$. While in the off-critical mixture, $N_A = 5,71,392$, $N_B = 1,90,464$, $\phi_A = 2.421 \times 10^{-1}$, $\phi_B = 7.265 \times 10^{-1}$, $\rho_A = 0.7265$, and $\rho_B = 2.179$. As the system is bound along the z-direction with two solid walls, the periodic boundary condition is applied only along x and y-directions. At the wall-polymer interfaces, the bounce-back boundary condition is applied [162]. Therefore, the polymer chains are restricted to penetrate the walls, and no-slip boundary condition is also produced along the z-direction with minimal interfacial density oscillation [163,164]. The walls also comprise DPD beads with density $\rho = 3$ and height $h = 1.0$. The the total number of wall beads are $N_w = 24,576$, so the volume fraction is $\phi_w = 3.125 \times 10^{-2}$.

First, we examine the reference scenario of zero shear rate to establish context for the discussion. In this initial case, the walls are stationary with no applied shear. To introduce shear, the walls are moved with velocities $\vec{v}_w = (v_{wx}, v_{wy}, v_{wz})$, where the y and z components are zero (v_{wy}, and $v_{wz} = 0$), allowing wall to move only in the x-direction with $v_{wx} = 0.1$, 0.5, and 1.0 and corresponding shear rates: $\dot{\gamma} = 1.56 \times 10^{-3}$, 7.80×10^{-3}, and 1.56×10^{-2}, respectively. We analyze three scenarios of applied shear: Case 2: Only the top wall moves in the positive x-direction. Case 3: Both the top and bottom walls move in the positive x-direction with identical velocities. Case 4: The walls move in

opposite x-directions (the top wall moves in positive x-direction, and the bottom wall in negative x-direction). Thus, the shear rate in our simulations ranges from $\dot{\gamma} = 1.8 \times 10^5/s$ to $1.8 \times 10^6/s$, aligning with the magnitude of shear rates used in microfluidic device experiments [165,166].

We investigate the phase separation kinetics of a polymer blend system using DPD simulations. Initially, the system is equilibrated for $t = 1 \times 10^5$ at $T = 5$ to achieve a homogeneously mixed or uncorrelated state. During this equilibration phase, no external shear is applied. Subsequently, we quench the temperature below the critical value. The time measure is reset to $t = 0$, and shear is introduced to the system. For ensemble averaging of the scaling functions and growth laws, we performed five independent runs. A more extensive ensemble averaging over ten runs was conducted to calculate the velocity profile and viscosity.

5.3 Critical mixture of polymer blend

First, we discuss the velocity profile generated in the system and the viscosity variation due to external shear that arises from moving walls. Since the shear implementation for both blends are the same, we have omitted the results for off-critical mixtures for brevity. Shear is applied by giving velocity (v_{wx}) to the wall beads along the x-direction, making the x-component of velocity v_x crucial for the system's velocity profile. In Fig. 5.1(a), we plot the average velocity profile $\langle v_x \rangle$ along the z-direction. Different symbols in the legend represent cases 2-4 studied here. The velocity profile is shown for $\dot{\gamma} = 1.56 \times 10^{-2}$ at $t = 1.2 \times 10^3$. First, the solid black line highlights the velocity profile for the reference ($\dot{\gamma} = 0$) case. Here, $\langle v_x \rangle = 0.0$ demonstrates the conservation of linear momentum. Black, red, and green symbols show the velocity profile data for $\dot{\gamma} \neq 0$. In case 2, $\langle v_x \rangle$ decreases with distance from the upper wall, illustrating a reduced shear effect in successive layers. The curve crosses zero around $z \simeq 48$ and decreases to a minimum negative value near

$z \simeq 24$. As the bottom wall is fixed, we notice $\langle v_x \rangle \to 0$ as $z \to 0$. In case 3, the effect of shear diminishes with increasing distance from the walls. Consequently, the velocity profile reaches a minimum negative value around $z \simeq L/2$. In case 4, the green curve grows linearly from the bottom to the top wall, crossing zero at $z \simeq L/2$. Velocity profile varies with the direction of wall motion in each case. These profiles demonstrate the fundamental principles of momentum conservation in fluid dynamics (in DPD simulation).

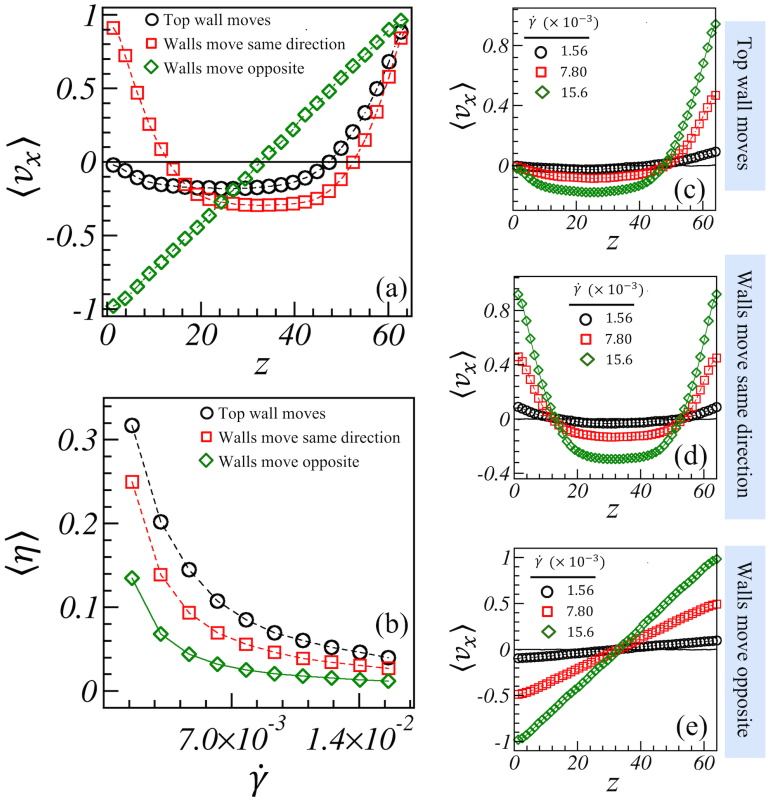

Fig. 5.1: (a) Variation of average velocity profile $\langle v_x \rangle$ along z-direction for all cases mentioned in the legends. The data is plotted for a fixed shear rate $\dot{\gamma} = 1.56 \times 10^{-2}$ at $t = 1.2 \times 10^3$. (b) Comparision of shear viscosity $\langle \eta \rangle$ as a function of $\dot{\gamma}$ at $t = 1.2 \times 10^3$. (c-e) $\langle v_x \rangle$ vs. z for different shear rates for cases 2-4, respectively.

In Fig. 5.1(b), we plot the average shear viscosity $\langle \eta \rangle$ against the shear rate $\dot{\gamma}$ at $t = 1.2 \times 10^3$. Different symbols in the legend represent cases 2-4 of this study. The notation $\langle ... \rangle$ denotes the ensemble average over ten simulation runs. A similar pattern in viscosity is observed in all cases, decreasing with an increase in shear rate. This behavior

indicates shear thinning, leading to the saturation of domains at lower $R(t)$ values at high shear rates. Comparing cases 2-4, the shear effect is most prominent in the last case, which shows the lowest shear viscosity.

The next notable point is the appearance of negative values in the velocity profile. In Figs. 5.1(c)-5.1(e), we compare the average velocity profiles for cases 2-4 at different shear rates as indicated in the legends. Due to wall motion, a flow field is generated in the adjacent slab of polymer fluids. The shear effect is greatest near the moving walls and decreases with distance. It eventually decays to zero at certain distances: around $z \simeq 48$ in case 2 (Fig. 5.1(c)), $z \simeq 12$ and $z \simeq 53$ in case 3 (Fig. 5.1(d)), and $z \simeq L/2$ in case 4 (Fig. 5.1(e)). The system exhibits characteristics of incompressible Newtonian flow, responding to non-equilibrium conditions by accommodating momentum flow in opposite directions to maintain momentum conservation within the system [167,168,171]. In case 1, momentum conservation is inherent in the DPD simulation by default. In case 2, the motion of the top wall applies shear to the system, causing neighboring layers to start sliding over each other. The average velocity of particles in different layers is highest near the upper wall and zero near the fixed bottom wall. To conserve the linear momentum, the net flow in the system must be zero. Therefore, the faster flow in the upper region is offset by a slower flow in the lower part of the box. Consequently, the negative value is present in the velocity profile with values lower than the average velocity of the particles. Consequently, a velocity gradient is generated along the vertical direction. In case 3, the velocity gradient is generated along the z-direction with maximum values near the walls and minimum negative values in the center, preserving linear momentum conservation within the system. In case 4, the net flow is balanced due to the equal and opposite directions of applied shear. Consequently, linear growth in the velocity profile is observed from bottom to top, crossing zero near $z \simeq L/2$ [167,168,171]. The generated momentum

increases as the shear rate increases. This causes the more pronounced negative values in the velocity profile, as shown in Figs. 5.1(c)-5.1(e) [167,168,171].

5.3.1 Case 1: Both walls fixed

We begin discussing the shear effect with a reference study where the applied shear rate is set to zero. Here, both walls are stationary, and we monitor domain coarsening over time. Fig. 5.2(a) and 5.2(b) represent the evolution morphologies at $t = 0$ and $t = 1.2 \times 10^3$. The red, yellow, and olive colors represent A, B, and wall beads, respectively. The intensity plot for the structure factor corresponding to the evolution at $t = 1.2 \times 10^3$ is shown in Fig. 5.2(c) along the xz-plane. This indicates slight anisotropy in the system due to the presence of two solid walls, as evidenced by the imperfect circle in the intensity plot, unlike in isotropic systems.

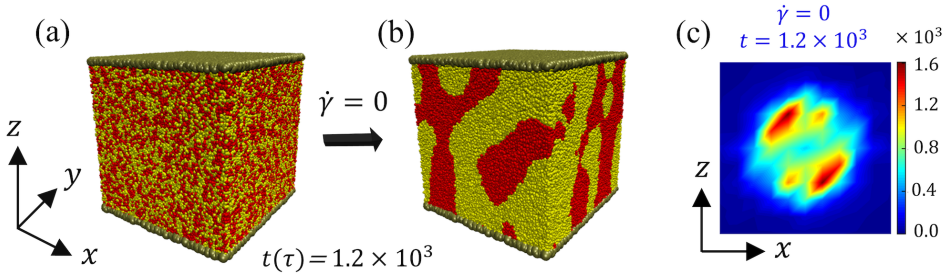

Fig. 5.2: The evolution snapshots are shown at $t = 0$ in (a) and $t = 1.2 \times 10^3$ in (b); the red, yellow, and olive colors represent the A, B, and wall-type beads, respectively. (c) The spatial intensity variation of $S(k_x, k_z)$ at $t = 1.2 \times 10^3$ along xz-plane.

In Fig. 5.3(a), we compare RDF $g_{AB}(r)$ vs. r at different time intervals mentioned in the legends. As time passes, separate A and B type clusters form, indicated by the broadening peaks and their shift toward higher r values. At later time intervals, the green and blue curves show increased peak amplitudes, indicating more organized domains in the later stages. To further characterize the evolved morphologies, we plot $C(r, t)$ vs. $r/R(t)$ in Fig. 5.3(b) for four different times, denoted by various symbols in the legends. The solid black line highlights the zero crossing of the correlation function.

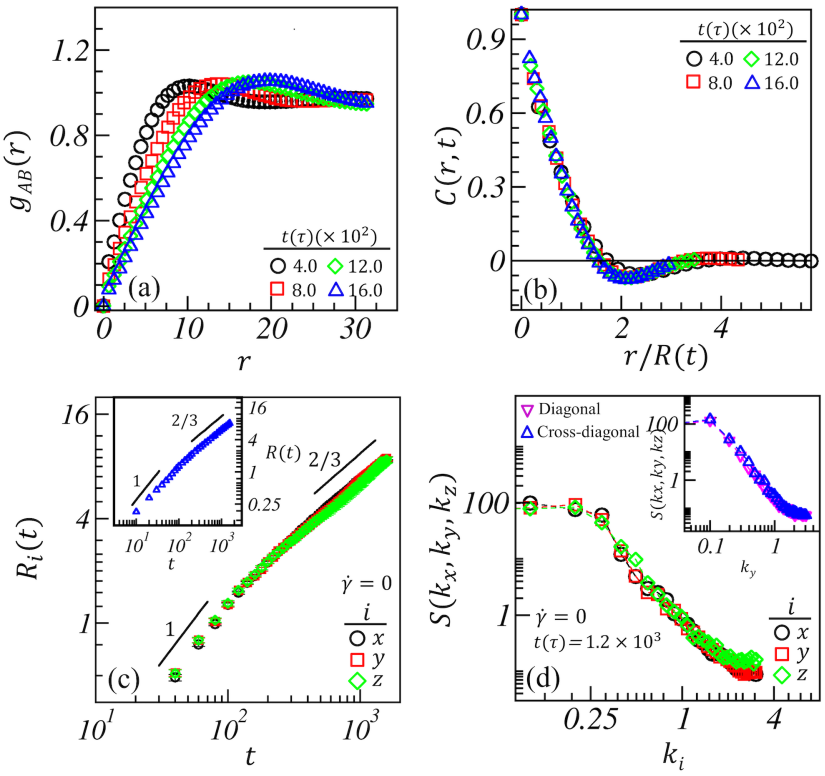

Fig. 5.3: (a) The RDF $g_{AB}(r)$ vs. r is compared at different time steps for zero shear rate. (b) The scaled correlation function $C(r,t)$ vs. $r/R(t)$. The solid black line represents the zero crossing. (c) The characteristic domain growth $R(t)$ against time is plotted after averaging along x, y, and z directions, as shown in the legends. The inset figure represents the spherically averaged length scale, $R(t)$ vs. t. Solid black lines with slopes 1 and 2/3 represent the viscous and inertial hydrodynamic growth laws. (d) The unidirectional structure factor $S(k_x, k_y, k_z)$ as a function of k_x, k_y, and k_z. The inset correspond to $S(k_x, k_y, k_z)$ vs. k_y along diagonal and cross-diagonal directions.

The correlation curves plotted with red, green, and blue symbols show excellent overlap, indicating a dynamical scaling regime. However, the early time data plotted with black symbols deviates slightly. The tail of the correlation curves ends at shorter distances, as the domain size increases over time..

The average domain size $R(t)$ vs. t is displayed in the inset of Fig. 5.3(c). The solid lines with slopes of 1 and 2/3 represent viscous and inertial hydrodynamic growth, respectively. As DPD is well-known to preserved the hydrodynamic behavior of the fluid system, the diffusive growth regime in short-lived. Therefore, we notice a crossover

from viscous to inertial hydrodynamic growth. Further, we plot the length scale along three different directions, as shown with the black, red, and green symbols in Fig. 5.3(c). Similar growth exponents are noted along different directions, with a crossover from the viscous ($\phi \sim 1$) to inertial hydrodynamic ($\phi \sim 2/3$) growth regime. However, as indicated in the intensity plot, a slight deviation from complete overlap at late times confirms the existence of a small degree of structural anisotropy in the system.

In Fig. 5.3(d), we plot the unidirectional structure factor $S(k_x, k_y, k_z)$ vs. k_x, k_y, and k_z with black, red, and green curves, respectively. Slight anisotropy develops in the system due to the non-periodic boundary condition along the z-direction, which is evident from the tiny deviation from overlapping the structure factor curves along different directions. The inset shows the variation of $S(k_x, k_y, k_z)$ vs. k_y along diagonal and cross-diagonal directions on the yz-plane. Along these directions, we observe a good overlap in the data, indicating the formation of an isotropic pattern.

5.3.2 Case 2: Only top wall moves

Here, we have introduced shear to the system by imparting velocity to the top wall. The bottom wall stays immobile. The velocity imparted to the top wall along positive x-direction determines the shear rate applied to the system. The results are compared at three different values of shear rate: $\dot{\gamma} = 1.56 \times 10^{-3}$, 7.80×10^{-3}, and 1.56×10^{-2}.

First, we plot the evolution images in $3d$ and the $2d$ cross-section of the xz-plane at $y = 32$ in Figs. 5.4(a)-5.4(c) for the different shear rates indicated. Upon the application of shear, the polymer chains realign themselves along the flow to minimize its impact. In the previous chapter, we examined a BCP melt system and observed the formation of lamellar morphology due to bond constraints between incompatible blocks. In contrast, separate A and B type chains are present in the polymer blend system. Therefore, under the influence of shear, polymer chains in the adjacent layers close to the top wall flow

along the direction of the wall velocity. The shear affects the successive layers in the bulk, causing them to move accordingly. At the minimal shear rate of $\dot{\gamma} = 1.56 \times 10^{-3}$, only a few layers from the top are influenced by the moving walls, resulting in the formation of an interconnected morphology at $t = 1.2 \times 10^3$. At $\dot{\gamma} = 7.80 \times 10^{-3}$ and 1.56×10^{-2}, the effect of shear is enhanced, and we observed that the evolving domains are aligning in the direction of the flow, and orientational order in the domains is observed in the upper half of the system. Thus, the system seems to develop lamellar-type morphology, particularly closer to the moving wall, which was not noticed in the reference system.

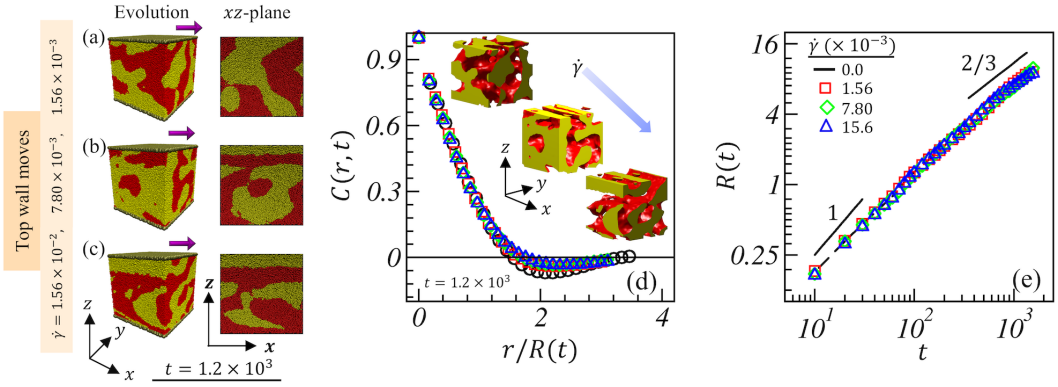

Fig. 5.4: (a-c) The evolution snapshots and corresponding xz-cross section are displayed for case 2 with different shear rates: (a) $\dot{\gamma} = 1.56 \times 10^{-2}$, (b) $\dot{\gamma} = 7.80 \times 10^{-3}$, and (c) $\dot{\gamma} = 1.56 \times 10^{-3}$. Related isosurfaces are also provided in the inset of (d). (d) and (e) show $C(r,t)$ vs. $r/R(t)$ and $R(t)$ vs. t, respectively, for different shear rates at $t = 1.2 \times 10^3$. The solid black lines in (e) represent the growth laws followed by $R(t)$.

To characterize the evolved morphologies shown in Figs. 5.4(a)-5.4(c), we plot $C(r,t)$ vs. $r/R(t)$ in Fig. 5.4(d) for the various shear rates at $t = 1.2 \times 10^3$. The isosurfaces corresponding to the evolutions depicted in Figs. 5.4(a)-5.4(c) are also displayed in the inset of Fig. 5.4(d). The yellow color represent the B-type beads and the blank space corresponds to A-type clusters. The black curve illustrates the correlation function for case 1 as a reference. There is an excellent overlap in the data shown in red ($\dot{\gamma} = 1.56 \times 10^{-3}$), green ($\dot{\gamma} = 7.80 \times 10^{-3}$), and blue ($\dot{\gamma} = 1.56 \times 10^{-2}$) curves, indicating the same universality classes. Additionally, the correlation functions at higher shear

rates exhibit smaller amplitude oscillations after the zero crossing. The reason could be the elongation of domains along the shear flow, leading to a reduction in the number of interfaces in the flow direction, specifically in the x-direction closer to the moving wall.

In Fig. 5.4(e), we compare $R(t)$ vs. t for different applied shear rates. As in case 1, we observe the expected behavior-a crossover from viscous to inertial hydrodynamic growth for all $\dot{\gamma}$ values. We notice the minimal variation in the behavior of average domain sizes over time. In this case, the primary change is confined to the alteration in the internal structural ordering, i.e., the domains close to the moving walls are aligned in the flow direction. Therefore, we can conclude that morphologies are different from the usual bicontinuous structure depending on the strength of the shear rate.

5.3.3 Case 3: Both walls move in the same direction

In this case, we allow both walls to move in the same direction (the positive x-direction) with similar velocities. The evolution snapshots and corresponding xz-cross section plots are displayed in Figs. 5.5(a)-5.5(c) at the late time $t = 1.2 \times 10^3$ for different shear rates indicated on the left. The related isosurfaces are also plotted in the inset of Fig. 5.5(d) to visualize the internal bulk morphology. At $\dot{\gamma} = 1.56 \times 10^{-3}$, only a few layers close to the moving walls are affected by shear. This effect enhanced up to the multiple layers in bulk with higher shear rates, forming elongated and more ordered domain patches over the given time intervals (see Figs. 5.5(b)-5.5(c)).

To characterize the domain evolution, we compare $C(r,t)$ vs. $r/R(t)$ in Fig. 5.5(d) at the late time $t = 1.2 \times 10^3$. The black curve shows the scaled correlation function for the reference case, i.e., for $\dot{\gamma} = 0.0$. Upon the application of shear ($\dot{\gamma} \neq 0.0$), the excellent overlap in the red, green, and blue curves represents the same statistical behavior for all $\dot{\gamma}$ values. Under the effect of shear, domains reorganize themselves along the flow

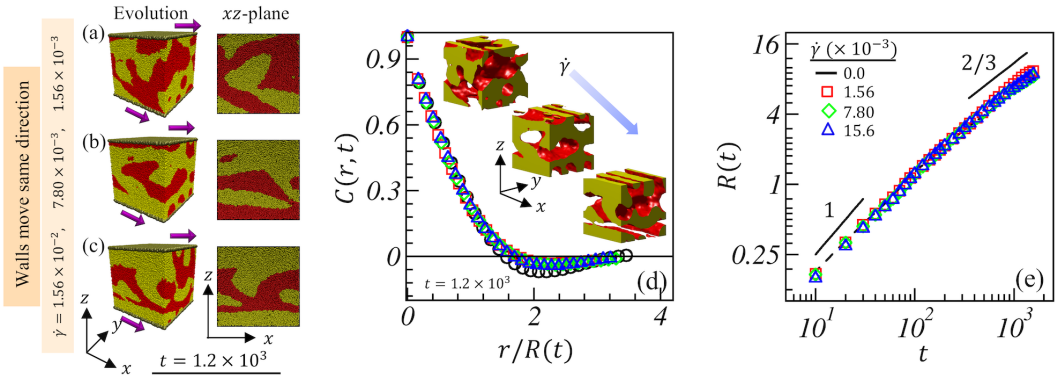

Fig. 5.5: The evolution snapshots for case 3 and corresponding xz-cross-section plots at $t = 1.2 \times 10^3$ is dispayed in (a-c) with different shear rates mentioned alongside them. Related isosurfaces are also provided in the inset of (d). Data for $C(r,t)$ vs. $r/R(t)$ and $R(t)$ vs. t are plotted in (d) and (e), respectively, for different shear rates shown in the legends at $t = 1.2 \times 10^3$. The solid black lines in (e) represent the growth laws followed by $R(t)$.

direction to minimize its impact. This results in smaller amplitude oscillations of the correlation function for $\dot{\gamma} \neq 0.0$ cases.

In Fig. 5.5(e), we plot the average length scale $R(t)$ vs. t for different shear rates mentioned in the legends. A crossover from viscous to inertial hydrodynamic growth is noted for all shear rates. The length scale data overlap suggests that the effect of the shear rate on the domain growth rate of the polymer blend system is negligible. However, more organized domains are formed in this case after the same time interval due to the increased effectiveness of the applied shear.

5.3.4 Case 4: Both walls move in opposite directions

In case 4, both walls are allowed to move in opposite directions. This opposite direction of applied shear facilitates a more rapid readjustment of the domains. Consequently, we notice more ordered A and B type clusters aligned parallel to the walls. The evolution snapshots are plotted in Figs. 5.6(a)-5.6(c) at the late time, $t = 1.2 \times 10^3$ for different shear rates. At high shear rates of $\dot{\gamma} = 7.80 \times 10^{-3}$ and 1.56×10^{-2}, more organized

domains are noted in the direction of the flow due to the effect of shear affecting more layers of the polymer fluids in bulk. However, at $\dot{\gamma} = 1.56 \times 10^{-3}$, the shear influences only a few layers close to the walls, resulting in domains that are not perfectly aligned and form an interconnected structure. In Fig. 5.6(b), a distorted lamellar structure is noted, while at the high shear rate in Fig. 5.6(c), a more phase-separated structure aligned along the xz-plane is noted. In Fig. 5.6(d), we plot the corresponding isosurfaces in the inset, representing the structures formed in the bulk of the system.

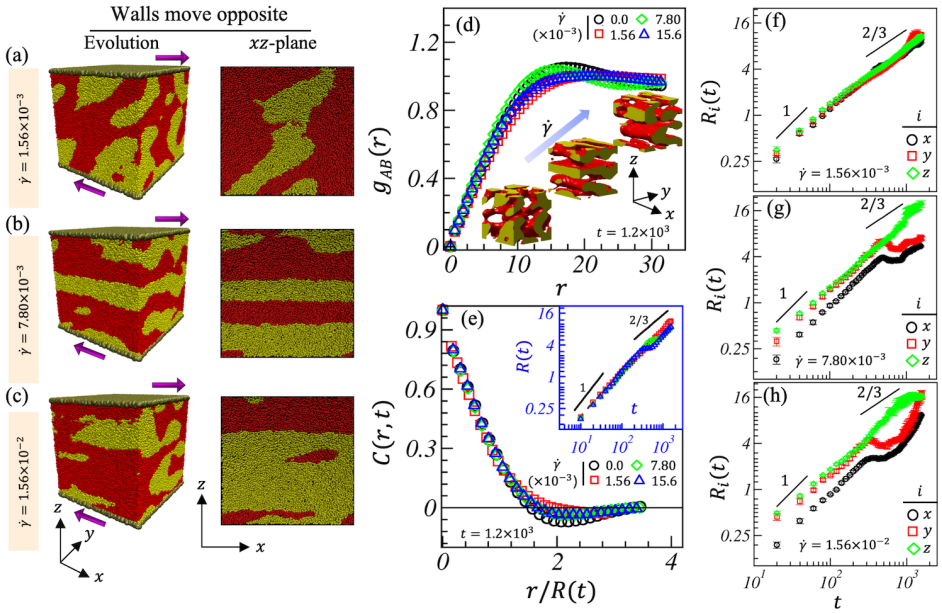

Fig. 5.6: (a-c) The evolution morphology and corresponding xz-cross section plots for the middle layer ($y = 32$).These are the snapshots at the late time intervals $t = 1.2 \times 10^3$ for different shear rates mentioned alongside them. (d) $g_{AB}(r)$ vs. r for different $\dot{\gamma}$ values. Inset represents the isosurfaces corresponding to the evolution pictures given in (a-c). (e) $C(r,t)$ vs. $r/R(t)$ is plotted for the same data set as in (d). The respective plots for $R(t)$ vs. t averaged along the radial direction are illustrated in the inset of (e). (f-g) The average length scale along different directions is plotted for various $\dot{\gamma}$ values. Solid lines with slopes 1 and 2/3 represent the viscous and inertial hydrodynamic growth laws followed by the system.

We compare the radial distribution function (RDF) in Fig. 5.6(d) at $t = 1.2 \times 10^3$. The RDF curves quantify the evolutions and illustrate how the particles are distributed over the space. The higher peak in the black curve corresponds to the A and B type

clusters evolved over time. In the evolution plotted in Fig. 5.6(a), a distorted structure is noted due to the low shear rate applied to the system. This leads to a smaller RDF peak shifted towards higher r values in the red curve at $\dot{\gamma} = 1.56 \times 10^{-3}$. At $\dot{\gamma} = 7.80 \times 10^{-3}$, the distorted lamellar morphology is formed in Fig. 5.6(b) aligned paralled to the wall. Consequently, a higher RDF peak is noted in the green curve, corresponding to the periodic distorted lamellar slabs. At $\dot{\gamma} = 1.56 \times 10^{-2}$, the smaller peak in the blue curve corresponds to a more phase-separated structure elongated in the flow direction at a high shear rate.

In Fig. 5.6(e) we plot $C(r,t)$ vs. $r/R(t)$ at different $\dot{\gamma}$ values, as discussed in Fig. 5.6(d) at $t = 1.2 \times 10^3$. The zero crossing is highlighted with a solid black line. The universal scaling behavior is noted in the late-time correlation at $\dot{\gamma} = 7.80 \times 10^{-3}$ (green curve) and 1.56×10^{-2} (blue curve). The black curve represents the formation of interconnected macrodomains for the given time intervals in the reference case. However, the tail of the red curve shifts to a shorter r value due to the formation of a distorted morphology at $\dot{\gamma} = 1.56 \times 10^{-3}$; these two curves clearly deviate from the universality class of the system at higher shear rates. At high shear rates, depicted by the green and blue curves, the domains are aligned parallel to the walls, resulting in smaller dips and longer tails in the correlation curves.

The inset of Fig. 5.6(e) represents the time-dependent average length scale for different shear rates. Here, the domain length is plotted along the radial direction. At different $\dot{\gamma}$ values, $R(t)$ follows the expected crossover from viscous to inertial hydrodynamic growth. At high shear rates, a dip is noted in the length scale due to the reorientation of the domains as a consequence of the effect of the moving walls. As the shear is effective in the bulk of the system, the reorientation of domains tends to dominate over coarsening, resulting in slow growth for a short period. Later, the length scale grows further, following the inertial regime.

To emphasize the dip in the curve, we have plotted the average domain growth separately along different directions in Figs. 5.6(f)-5.6(h) for $\dot{\gamma} = 1.56 \times 10^{-3}$, 7.80×10^{-3}, and 1.56×10^{-2}, respectively. Since, we observe the interconnected morphology at $\dot{\gamma} = 1.56 \times 10^{-3}$, the corresponding directional length scales, plotted in Fig. 5.6(f) with black, red, and green curves along the x, y, and z directions, respectively, show a good data overlap with minimal deviation, representing the small anisotropy developed in the system. At high shear rates of $\dot{\gamma} = 7.80 \times 10^{-3}$ and 1.56×10^{-2}, anisotropy develops in the system, showing different behaviors in different directions. The external shear leads to the formation of ordered structures oriented along the xy-plane. Consequently, at the point where the shear dominates over the domain coarsening, a dip in the length scale is observed along the x and y directions in black and red curves in Figs. 5.6(g)-5.6(h) due to the reorientation of domains. We notice further growth in these curves, which is more prominent in Fig. 5.6(h). We notice the typical polymer blend behavior in the green curve with a crossover from viscous to inertial hydrodynamic growth. No dip is noted in the length scale data along the z-direction because of more periodic interfaces perpendicular to the flow. The green curve shows saturation at the high shear rate in Fig. 5.6(h). As we increase the shear rate, the deviation in these curves also increases, illustrating the enhanced anisotropy in the system.

To further examine the anisotropy, we have plotted the scattering intensity of the structure factor along the xz-plane in Figs. 5.7(a)-5.7(d) for different shear rates at $t = 1.2 \times 10^3$. The color bar represents the range of scattering intensity. Due to the confinement of the system along vertical direction, a small anisotropy is present in the system in Fig. 5.7(a) ($\dot{\gamma} = 0.0$). Figs. 5.7(b)-5.7(d) shows the enhancement in anisotropy with the increase in shear rate. The appearance of elongated intensity in the x-direction justifies the formation of well-ordered morphologies along the xy-plane at high shear rates $\dot{\gamma} = 7.80 \times 10^{-3}$ and 1.56×10^{-2} as discussed in Figs. 5.7(c) and 5.7(d), respectively.

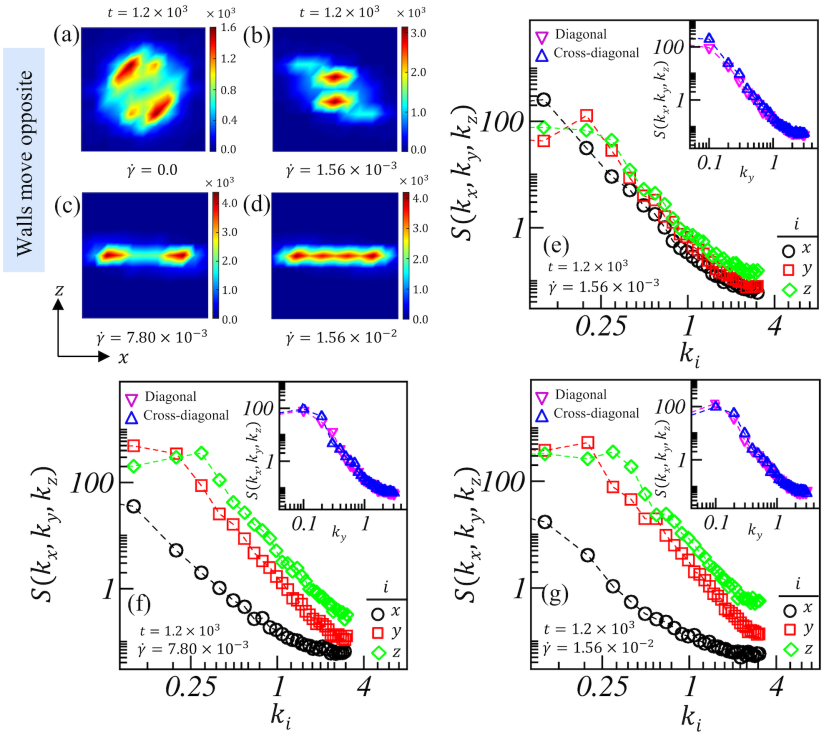

Fig. 5.7: (a-d) The spatial intensity variation of the structure factor $S(k_x, k_z)$ along xz-plane for different $\dot{\gamma}$ values at $t = 1.2 \times 10^3$. To see the structural anisotropy, the unidirectional structure factor $S(k_x, k_y, k_z)$ vs. k_x (black curve), k_y (red curve), and k_z (green curve) is plotted in (e), (f), and (g) for $\dot{\gamma} = 1.56 \times 10^{-3}$, 7.80×10^{-3}, and 1.56×10^{-2}, respectively. The magenta and blue curves demonstrate $S(k_x, k_y, k_z)$ vs. k_y along diagonal and cross-diagonal directions.

In Figs. 5.7(e)-5.7(g), we plot the unidirectional structure factor along the k_x, k_y, and k_z-directions, for different shear rates at $t = 1.2 \times 10^3$. At a low shear rate, the minimal deviation is noted in the structure factor curves along different directions in Fig. 5.7(e). This represents the development of small anisotropy in the system because the shear is not very effective in the bulk at $\dot{\gamma} = 1.56 \times 10^{-3}$. At $\dot{\gamma} = 7.80 \times 10^{-3}$, a distorted lamellar morphology is formed along the xy-plane. Therefore, primary peaks are not observed in the structure factor along the k_x and k_y directions in Fig. 5.7(f). We notice the black curve has a lower magnitude compared to the red one because the observed sheets are flatter along the x-direction. In Fig. 5.7(g), a more phase-separated structure develops due to a high shear rate by the same time interval. Here, the structure factor follows

the same pattern; elongated domains are observed along the xy-plane, while periodicity is observed along the z direction. The inset of Figs. 5.7(e)-5.7(g) depicts the structure factor along diagonal and cross-diagonal directions in the yz-plane with magenta and blue curves, respectively. Similar patterns are formed along these directions, resulting in good overlap in the structure factor for each $\dot{\gamma}$ value.

5.4 Off-critical mixture of polymer blend

After the comprehensive study on the critical polymer blend system, we are now interested in examining the effect of shear on an off-critical polymer blend system with a $3:1$ ratio of A and B-type beads. In this system, we will investigate all cases of applied external shear one by one, as discussed earlier.

5.4.1 Case 1: Both walls fixed

We will follow a similar pattern for the discussion as for the critical mixture. In case 1, both walls are stationary, and no shear is applied to the system. We have plotted the evolution pictures at $t = 0$ and $t = 1.2 \times 10^3$ in Figs. 5.8(a) and 5.8(b). Corresponding to the late-time evolution at $t = 1.2 \times 10^3$, we have plotted the spatial variation of the intensity of the structure factor along the xz-plane in Fig. 5.8(c). Due to the confinement of the system along the z-direction, we observe the formation of anisotropic domains. This anisotropy results in the appearance of distinct intensity peaks in the intensity plot along the z-direction.

Additionally, we plot the RDF curves in Fig. 5.9(a) to quantify the evolution at different time intervals. As time progresses, domain coarsening is indicated by the broadening of RDF peaks and their shift towards higher r values. Additionally, the height of the peaks increases due to the formation of more ordered A and B-type clusters. In Fig.

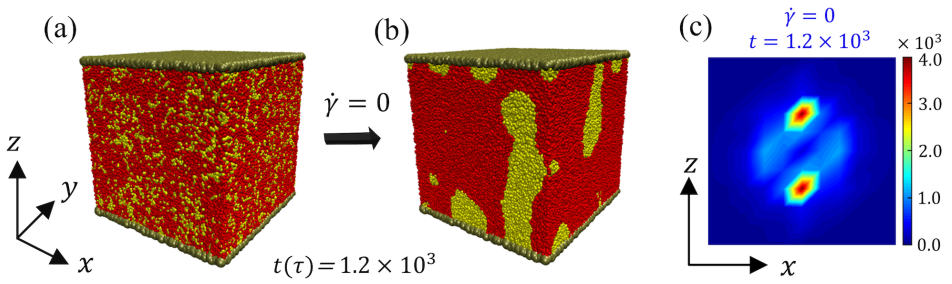

Fig. 5.8: The evolution snapshots are shown at $t = 0$ in (a) and $t = 1.2 \times 10^3$ in (b). (c) The spatial intensity variation of $S(k_x, k_z)$ at $t = 1.2 \times 10^3$ along xz-plane.

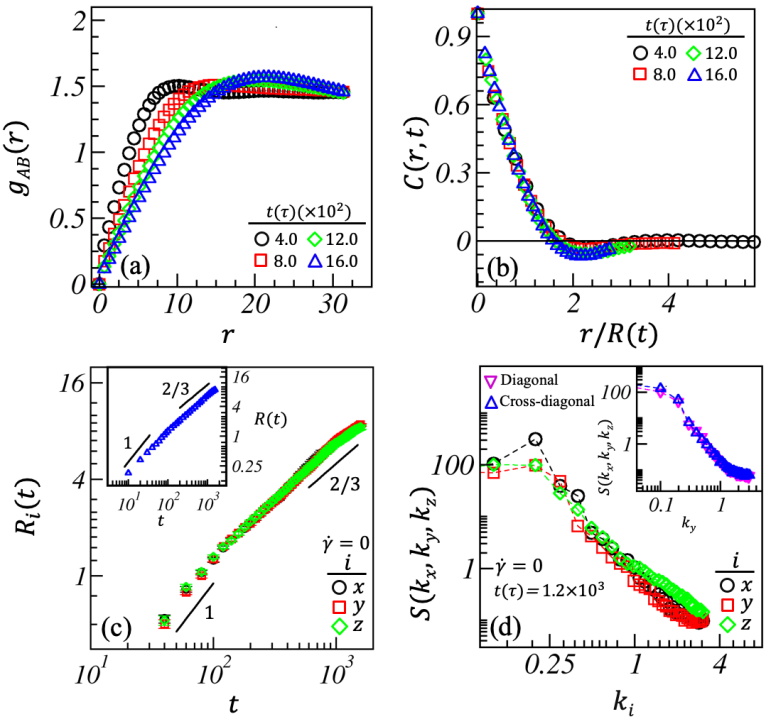

Fig. 5.9: Off-critical polymer mixture with ratio $A : B = 3 : 1$: (a) $g_{AB}(r)$ vs. r at various time steps mentioned in the legends. (b) Plots for $C(r,t)$ vs. $r/R(t)$ for the same data set used in (a). (c) Characteristic length scale $R(t)$ vs. t is represented along different directions with various symbol types in the legends. Inset plots the time-dependent spherically averaged domain length. (d) Plots for $S(k_x, k_y, k_z)$ as a function of k_x, k_y, and k_z, representing the anisotropy along different directions. In the Inset, the magenta and blue curves plot $S(k_x, k_y, k_z)$ vs. k_y along diagonal and cross diagonal directions on xz-plane.

5.9(b), we have plotted $C(r,t)$ vs. $r/R(t)$ for different time intervals, as mentioned in the legends. The domain evolution over time results in the termination of the correlation function at shorter distances. We observe deviations from the scaling behavior in these

curves. In the blue curve, a deeper dip after the zero crossing indicates the formation of an ordered structure at a later stage in off-critical mixture.

To discuss the growth laws, we have plotted $R(t)$ vs. t in Fig. 5.9(c). The inset shows the spherically averaged domain size, representing the typical macroscopic behavior of a polymer blend system. The length scale transitions from viscous ($\phi \sim 1$) to inertial ($\phi \sim 2/3$) hydrodynamic regime. The black, red, and green curves depict the variation of the average domain size along all three axes. There is minimal deviation in these curves, but each has the same growth exponent. This anisotropic characteristic arises due to the presence of two solid walls in the system.

Furthermore, we plot $S(k_x, k_y, k_z)$ along the k_x, k_y, and k_z directions in Fig. 5.9(d). The distinct behavior of the structure factor along different directions indicates the anisotropy developed in the system. The inset shows $S(k_x, k_y, k_z)$ vs. k_y along diagonal and cross-diagonal directions using magenta and blue curves, respectively. The good overlap in these data indicates isotropic behavior in these directions.

5.4.2 Case 2: Only top wall moves

Now, we move to the second case, where only the top wall is allowed to move in the positive x-direction. The layers adjacent to the top wall start flowing along the shear direction. With an increase in shear rate, the wall motion influences more layers of the polymer fluids in the bulk. As explored in context of a critical mixture, when shear is applied, phase-separating domains attempt to align themselves along a specific direction to minimize the impact of shear. We have plotted the evolution snapshots at $t = 1.2 \times 10^3$ in Figs. 5.10(a)-5.10(c) for different shear rates: $\dot{\gamma} = 1.56 \times 10^{-3}$, 7.80×10^{-3}, and 1.56×10^{-2}. Corresponding cross-sectional plots along the xz-plane for $y = 32$ are also plotted beside them. These snapshots suggest that the shear predominantly impacts the upper part of the system, and its effect increases with the shear rate. At high shear rates,

elongated domains are formed along the shear direction. To examine the bulk structure, we have plotted the isosurfaces related to these snapshots in the inset of Fig. 5.10(d).

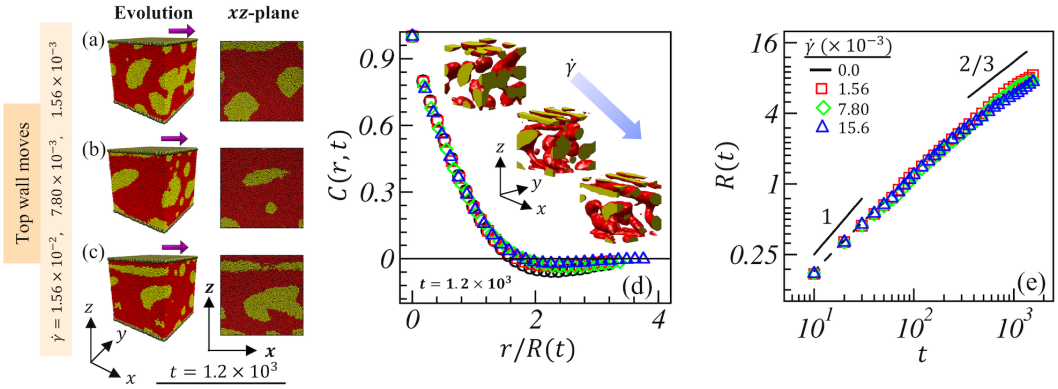

Fig. 5.10: (a-c) Domain evolution and $2d$ cross-section plots along xz-plane for the case 2. These pictures are related to different shear rates mentioned at left for the late time $t = 1.2 \times 10^3$. Related isosurfaces are also plotted in the inset of (d). (d) Scaled correlation as a function of $r/R(t)$ for the same case as in (a-c). The corresponding time-dependent average domain size is plotted in (e). $R(t)$ curves follow the viscous and inertial hydrodynamic growth represented by solid black lines with slopes 1 and 2/3, respectively.

To characterize the evolved morphology, we have plotted $C(r,t)$ against $r/R(t)$ in Fig. 5.10(d) for different shear rates, at $t = 1.2 \times 10^3$. As the shear rate increases, the impact of shear leads to the formation of more ordered structures forming elongated domains along x-direction. Consequently, smaller amplitude oscillations are noted after zero crossing in the correlation function curves at high shear rates. The non-overlapping curves for different shear rates indicate deviation from universal scaling behavior. Additionally, we have plotted the time-dependent average domain size $R(t)$ vs. t in Fig. 5.10(e) for different $\dot{\gamma}$ values. The length scale curves transition from an early-time viscous hydrodynamic regime ($\phi \sim 1$) to inertial hydrodynamic growth ($\phi \sim 2/3$). At all shear rates, the length scale follows a similar behavior. Still, as the shear rate increases, the growth rate diminishes later due to shear thinning behavior, as discussed in the viscosity plot depicted in Fig. 5.1.

5.4.3 Case 3: Both walls move in the same direction

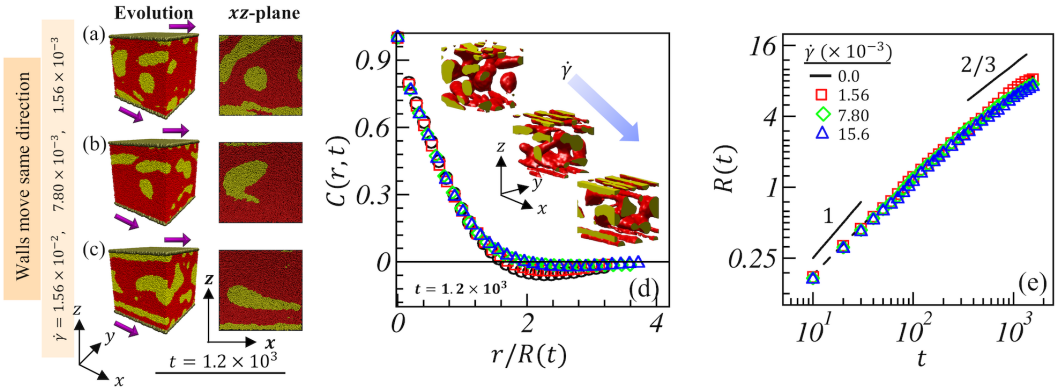

Fig. 5.11: (a-c) Evolution snapshots and corresponding xz-cross section plots for $y = 32$ at $t = 1.2 \times 10^3$. Related isosurfaces are also shown in the inset of (d). (d) Comparison of Scaled correlation $C(r,t)$ vs. $r/R(t)$ corresponding to the evolutions plotted in (a-c). (e) $R(t)$ vs. t for different shear rates mentioned in the legends. Solid black lines with slope 1 and 2/3 represent the growth laws followed by $R(t)$.

In this scenario, both walls are moving in the positive x-direction to apply shear on the system. In Figs. 5.11(a)-5.11(c), we have plotted the evolution snapshots in $3d$ and corresponding xz-cross section plots of the $y = 32$ plane. These snapshots are taken at the late time interval $t = 1.2 \times 10^3$ for three different $\dot{\gamma}$ values: $\dot{\gamma} = 1.56 \times 10^{-3}$, 7.80×10^{-3}, and 1.56×10^{-2}. At $\dot{\gamma} = 1.56 \times 10^{-3}$, shear predominantly influences only a few layers near the walls, displaying an interconnected morphology akin to what is typically observed in standard polymer blend systems. However, with an increase in wall velocity, shear is more effective in the bulk of the system, leading to the formation of perfectly oriented domains along the xz-plane (see Figs. 5.11(b)-5.11(c)). Isosurfaces corresponding to these evolutions are shown in the inset of Fig. 5.11(d).

In Fig. 5.11(d), we have compared $C(r,t)$ vs. $r/R(t)$ for various shear rates as indicated in the legends. With an increase in shear, we notice the formation of more ordered elongated domains. This results in the appearance of a smaller dip and prolonged tails of the correlation function at high shear rates. Next, we have plotted the characteristic domain length in Fig. 5.11(e) for different shear rates. For different $\dot{\gamma}$ values,

the typical macroscopic phase separation is noted in the length scale curves, following a crossover from viscous ($\phi \sim 1$) to inertial ($\phi \sim 2/3$) hydrodynamic growth. Additionally, shear-thinning behavior is evident, leading to slower growth at later times, particularly at high shear rates.

5.4.4 Case 4: Both walls move in opposite directions

The impact of shear is more pronounced in this scenario due to the opposite motion of the walls. Consequently, more ordered structures are formed compared to the previous scenarios. The evolution snapshots for various shear rates are shown in Figs. 5.12(a)-5.12(c) at the late time intervals $t = 1.2 \times 10^3$. Corresponding $2d$ cross-section plots are also displayed alongside them for the middle layer of the xz-plane at $y = 32$. At the minimal shear rate of $\dot{\gamma} = 1.56 \times 10^{-3}$, shear is effective only in few layers near the walls. However, it fails to generate elongated structures along the x-direction, as observed in 5.12(b) and 5.12(c) within the specified time interval. At a high shear rate of $\dot{\gamma} = 1.56 \times 10^{-2}$, well-ordered structures are formed in Fig. 5.12(c) oriented along the flow direction. The isosurfaces corresponding to these snapshots are displayed in the inset of Fig. 5.12(d) to visualize the bulk structures. From these snapshots, we observe the formation of cylindrical structures at the high shear rate of $\dot{\gamma} = 7.80 \times 10^{-3}$, and 1.56×10^{-2}.

We further plot the RDF in Fig. 5.12(d) for different $\dot{\gamma}$ values depicted in the legends. In the reference black curve, the primary peak illustrates the formation of interconnected domains within specified time intervals. Upon applying minimal shear at $\dot{\gamma} = 1.56 \times 10^{-3}$ (red curve), the reorientation of the domains results in a decreased height of the prominent peaks. The green and blue curves exhibit primary peaks at smaller r values, accompanied by additional minor oscillations, illustrating the formation of cylindrical structures as depicted in Figs. 5.12(b) and 5.12(c). To characterize the evolution at different shear

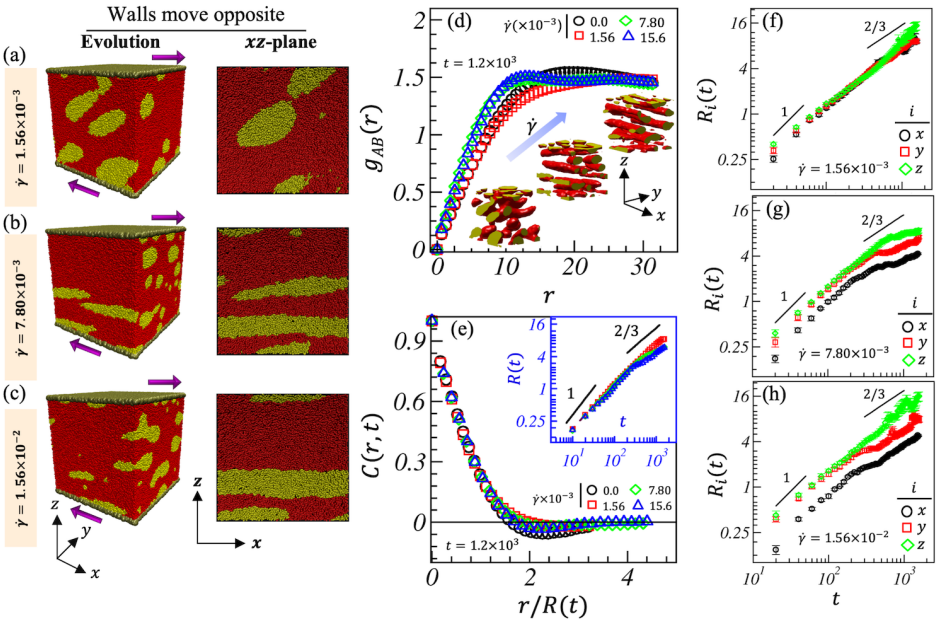

Fig. 5.12: (a-c) Plots for the late-time domain evolution and corresponding xz-cross section plots for $y = 32$ at different shear rates. (d) The RDF plots for different $\dot{\gamma}$ values at $t = 1.2 \times 10^3$. Inset represents the isosurfaces corresponding to the evolution pictures displayed in (a-c). (e) $C(r,t)$ vs. $r/R(t)$ for different shear rates, same as in (d). A solid black line depicts zero crossing. Inset represents the plots for $R(t)$ vs. t for different $\dot{\gamma}$ values. (f-h) $R(t)$ vs. t averaged along x, y, and z directions for different shear rates given in each figure. $R(t)$ curves show a cross-over from viscous to inertial hydrodynamic growth represented by solid lines.

rates, we plot the scaled correlation function in Fig. 5.12(e) at $t = 1.2 \times 10^3$. As discussed earlier, higher shear rates result in the formation of more ordered A and B type clusters over time. We notice the dip shifting towards lower r values in the correlation curves with increased shear rates due to the formation of elongated cylinders oriented along x-direction. However, the reference case follows the typical polymer blend behavior with isotropic domain evolution. Corresponding to the data plotted in Fig. 5.12(d)-5.12(e), we plot the characteristic domain growth over time in the inset of Fig. 5.12(e). For different $\dot{\gamma}$ values, a crossover from viscous ($\phi \sim 1$) to inertial ($\phi \sim 2/3$) hydrodynamic growth is noted. However, with increased shear rates, we observe the reorientation of the domains forming well-organized cylindrical structures along the x-direction. Due to the formation

of elongated structures along a particular direction, a dip in the length scale is noted. After that, the length scale grows further, but with an increase in shear rate, the growth diminishes due to shear thinning behavior.

We have plotted the $R(t)$ vs. t along the x, y, and z-directions in Figs. 5.12(f)-5.12(h) to highlight the slowdown of domain growth at high shear rates. To mitigate the impact of shear, domains start reorienting themselves in a specific direction. In the case of a critical mixture, we observed the formation of distorted lamellar structures along the xy-plane. In contrast, cylindrical domains are formed elongated along the x-direction for an off-critical mixture. Due to the formation of cylindrical domains along the x-direction, the likelihood of encountering another type of cluster diminishes significantly when moving along the x-direction. Consequently, we observe maximum deceleration of domain growth along this direction. Compared to the x-direction, we notice increased growth in the other two directions because there are more chances of encountering different types of clusters in these directions. Comparing the results for different shear rates plotted in Figs. 5.12(f)-5.12(h), the slowdown in $R(t)$ initiates at $t = 800$, 400, and 300 for $\dot{\gamma} = 1.56 \times 10^{-3}$, 7.80×10^{-3}, and 1.56×10^{-2}, respectively. This illustrates that the effect of shear dominates over domain coarsening earlier at higher shear rates. The non-overlapping nature of these curves signifies the development of anisotropy in the system due to the application of external shear.

Further, we plot the scattered intensity of the structure factor along the xz-plane for various shear rates in Fig. 5.13(a)-5.13(d). Due to non-periodicity along the vertical direction, we notice anisotropy even in the absence of external shear, resulting in two distinct peaks in the intensity plot in Fig. 5.13(a). Upon applying the external shear, more ordered structures oriented in the flow direction are observed. In the corresponding intensity plots displayed in Figs. 5.13(b)-5.13(d), the elongated intensity pattern is observed along the x-direction. To further demonstrate the anisotropy, we plot the

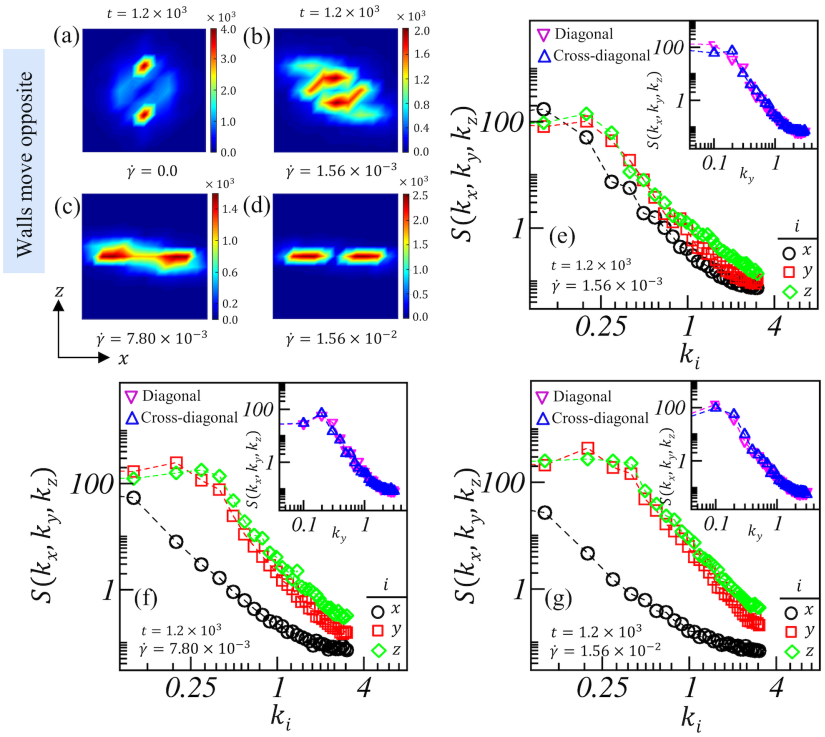

Fig. 5.13: (a-d) The intensity variation of the structure factor along xz-plane for different shear rates at $t = 1.2 \times 10^3$. Unidirectional structure factor $S(k_x, k_y, k_z)$ vs. k_x, k_y, and k_z is compared for $\dot{\gamma} = 1.56 \times 10^{-3}$ in (e), $\dot{\gamma} = 7.80 \times 10^{-3}$ in (f), and $\dot{\gamma} = 1.56 \times 10^{-2}$ in (g) at $t = 1.2 \times 10^3$. The inset of each picture depict the variation of structure factor as a function of k_y along diagonal and cross-diagonal directions.

structure factor along all three directions for $\dot{\gamma} = 1.56 \times 10^{-3}$, 7.80×10^{-3}, and 1.56×10^{-2} in Figs. 5.13(e)-5.13(g), respectively. With an increase in shear rate, the deviation of the black, red, and green curves increases, illustrating heightened anisotropy along different directions due to the formation of ordered structures. As the cylinders formed at high shear rates are elongated in the x-direction, the black curve diminishes, and primary peaks disappear due to a lack of periodicity along the x-axis. At the same time, the presence of high periodic peaks in the red and green curves represents the formation of more periodic structures along these directions at high shear rates. The insets of these figures plot the structure factor averaged along the diagonal and cross-diagonal directions along the yz-plane. We observe a good overlap in these curves, indicating isotropy along these directions, except for Fig. 5.13(e), where small anisotropic domains are present.

5.5 Summary and discussion

In this chapter, we study the phase separation kinetics of a polymer blend system under the influence of external shear using the DPD framework. We have examined both critical and off-critical polymer blend systems with compositions of $A : B = 1 : 1$ and $3 : 1$, respectively. We have considered periodic boundary conditions in the x and y directions, while the system is confined along the z-direction with two solid walls. Shear is applied to the system by imparting a specific velocity to the walls in a particular direction. Based on the wall motion, we have divided our study into four cases: (i) both walls are stationary, (ii) only the top wall moves in the positive x-direction. (iii) both walls move in the positive x-direction, and (iv) Both walls move in opposite directions. We study the impact of external shear on evolved morphology, scaling function, growth laws, and other relevant parameters. Additionally, we have calculated the velocity profile along the z-direction and the viscosity variation with shear rate to understand the effect of the moving walls on the bulk of the system.

Under the effect of moving walls, the polymer chains close to the walls start flowing along the shear direction. This effect intensifies in successive layers within the bulk of the system as the shear rate increases. Additionally, the phase-separating domains attempt to reorient themselves in a specific direction to mitigate the impact of shear. After considerable time intervals, we observe the formation of well-ordered domains elongated along a particular direction. In a critical mixture, distorted lamellar structures are formed, whereas distorted cylindrical domains are observed in an off-critical mixture.

Evolution images captured at varying shear rates show that elongated structures are aligned in a specific direction. These findings are justified by shifts in RDF peaks towards lower r values and reductions in the amplitude of oscillations beyond zero crossings in corresponding correlation function curves. Both systems exhibit typical polymer blend behavior, where the length scales transition from early-time viscous ($\phi \sim 1$) to late-time

inertial ($\phi \sim 2/3$) hydrodynamic growth across all shear rates. However, due to domain reorientation at higher shear rates, we observe a dip in domain growth for a short period. Additionally, we plotted average domain sizes along the x, y, and z directions, revealing non-overlapping data at high shear rates indicative of distinct growth rates along different axes due to the formation of ordered structures, and hence the anisotropic morphologies.

To investigate the emergence of anisotropy in the system, we analyzed the scattering intensity specifically along the xz-plane and the structure factor along all three axes. The elongated intensity observed along a specific direction and the non-overlapping nature of the structure factor curves across different directions indicate the formation of anisotropic domains under shear. Additionally, the decrease in average shear viscosity with increasing shear rate highlights the shear thinning behavior of the domains in response to external shear forces.

This study investigates the impact of shear induced by moving walls on polymer blend systems. We observed the formation of distorted lamellae and cylindrical structures, which are typically difficult to achieve in conventional blend systems. These outcomes have the potential to lay the groundwork for developing a versatile framework for generating diverse morphologies from polymeric systems, offering promising prospects for industrial applications.